

1 **Array-based iterative measurements of SmKS travel**
2 **times and their constraints on outermost core structure**

3 **Wenbo Wu^{1,2}, and Jessica C. E. Irving¹**

4 ¹ Department of Geosciences, Princeton University, Princeton, NJ 08541, USA

5 ²Seismological Laboratory, Division of Geological and Planetary Sciences, California Institute of
6 Technology, Pasadena, CA 91125, USA

7 **Key Points:**

- 8 • We develop an array-based iterative method to measure SmKS-SKKS (m=3-5)
9 differential travel times.
10 • 3D mantle structure effects must be considered in studies of SmKS differential travel
11 times.
12 • Our measurements support a low V_p at the top of outer core.

Corresponding author: Wenbo Wu, wenbow@caltech.edu

-1-

This article has been accepted for publication and undergone full peer review but has not been through the copyediting, typesetting, pagination and proofreading process which may lead to differences between this version and the Version of Record. Please cite this article as doi: 10.1029/2019JB018162

Abstract

Vigorous convection in Earth's outer core led to the suggestion that it is chemically homogeneous. However, there is increasing seismic evidence for structural complexities close to the outer core's upper and lower boundaries. Both body waves and normal mode data have been used to estimate a P-wave velocity, V_p , at the top of the outer core (the E' layer), which is lower than that in the Preliminary Reference Earth Model. However, these low V_p models do not agree on the form of this velocity anomaly. One reason for this is the difficulty in retrieving and measuring SmKS arrival times. To address this issue, we propose a novel approach using data from seismic arrays to iteratively measure SmKS-SKKS differential travel times. This approach extracts individual SmKS signal from mixed waveforms of the SmKS series, allowing us to reliably measure differential travel times. We successfully use this method to measure SmKS time delays from earthquakes in the Fiji-Tonga and Vanuatu subduction zones. SmKS time delays are measured by waveform cross-correlation (CC) between SmKS and SKKS and the CC coefficient allows us to access measurement quality. We also apply this iterative scheme to synthetic SmKS seismograms to investigate the 3D mantle structure's effects. The mantle structure corrections are not negligible for our data and neglecting them could bias the V_p estimation of uppermost outer core. After mantle structure corrections, we can still see substantial time delays of S3KS, S4KS and S5KS, supporting a low V_p at the top of Earth's outer core.

1 Introduction

The liquid outer core in the Earth plays a critical role in the geodynamo and in thermochemical interactions between the mantle and core. Seismic studies can provide important constraints on the physical properties of the core and therefore improve our understanding of the composition and state of the core (Hirose et al., 2013). Due to vigorous convection, the bulk of the outer core is believed to be well mixed and therefore chemically homogeneous (Stevenson, 1987). However, there is increasing seismic evidence for structural complexities close to its top and bottom boundaries. A stratified layer with a lower V_p gradient than the Preliminary Reference Earth Model (PREM; Dziewonski & Anderson, 1981), labeled the F-layer, has been documented using body seismic wave observations (Souriau & Poupinet, 1991b; Song & Helmberger, 1995; Zou et al., 2008; Ohtaki & Kaneshima, 2015). Another stratified layer, the E' layer, is hypothesized to

45 exist at the top of outer core and its properties may be constrained by geomagnetic sec-
46 ular variations (Gubbins, 2007; Buffett, 2014), but the seismic evidence, especially SmKS
47 differential arrival times, for this layer is contradictory and controversial (e.g. Eaton &
48 Kendall, 2006; Alexandrakis & Eaton, 2010; Helffrich & Kaneshima, 2010; Kaneshima
49 & Helffrich, 2013).

50 SmKS waves ($m=1, 2, 3, \dots$) travel as S-waves in the mantle, are converted to com-
51 pressional waves entering the outer core, reflected $m-1$ times on the underside of the core-
52 mantle boundary (CMB), and reconvert to S-waves to travel through the mantle (Fig.
53 1a). SmKS waves are sensitive to the structure of outer core and their arrival times have
54 been used to investigate V_p (compressional wave velocity) in the shallow outer core (Choy,
55 1977). SKS absolute arrival times have a large scatter, especially due to 3D mantle struc-
56 ture (e.g. Garnero et al., 2016), which results in large uncertainties in their constraints
57 on outer core structure. SKKS and SKS have similar raypaths near the source, so their
58 differential arrival times can partially remove the source effects and constrain the V_p of
59 shallow outer core better. Hales & Roberts (1971) compiled SKKS-SKS differential ar-
60 rival times and found a low V_p in the outermost core. However, the reliability of this
61 study is reduced by the uncorrected phase shifting between SKS and SKKS (Choy & Richards,
62 1975; Choy, 1977).

63 Although the ray paths of SKS and SKKS are close to each other near the source,
64 they diverge further in the lower mantle, where lateral heterogeneities could affect their
65 different travel times (Garnero et al., 1988; Souriau & Poupinet, 1991a). Compared to
66 SKKS and SKS, SmKS and $S(m-1)KS$ with $m>2$, e.g. S3KS-SKKS, have closer raypaths
67 (Fig. 1a) and therefore their differential arrival times are less affected by 3D mantle struc-
68 tures. With the high quality seismic data accumulated in the last few decades, many more
69 observations of SmKS ($m\geq 2$) waves has been reported and their differential travel times
70 have been used to investigate the stratification of the top outer core. However, the con-
71 clusions of various studies are not consistent. For example, Alexandrakis & Eaton (2007)
72 exploited the Empirical Transfer Function (ETF) technique to precisely measure SmKS
73 differential travel times and found no evidence for stratification, consistent with some
74 other SmKS studies (e.g. Souriau & Poupinet, 1991a; Alexandrakis & Eaton, 2010). In
75 contrast, other reports support a layer with lower V_p than that of PREM in the outer-
76 most core (e.g. Garnero et al., 1993; Tanaka, 2004; Eaton & Kendall, 2006; Tanaka, 2007;
77 Helffrich & Kaneshima, 2010; Kaneshima & Helffrich, 2013; Tang et al., 2015; Kaneshima

78 & Matsuzawa, 2015; Kaneshima, 2018), although the thickness and amplitude of the Vp
79 anomaly varies from one study to another.

80 There are at least two reasons for the preceding contradictory results. The first one
81 is the difficulty in extracting each individual SmKS phase and precisely measuring the
82 differential arrival times. For high orders $m \geq 3$, SmKS series constitute a whispering-
83 gallery mode and consecutive SmKS phases have very close arrival times (e.g. S4KS and
84 S5KS in Fig. 1a), which makes separating consecutive SmKS waveforms difficult. An-
85 other problem is contamination from lateral heterogeneities in mantle structure. Although
86 ray paths of SmKS and S(m-1)KS ($m > 2$) series are closer to each other than that of SKS
87 and SKKS, there are still differences in the mantle, especially the heterogeneous D'' re-
88 gion (Garnero & Helmberger, 1995). These mantle heterogeneities could cause large un-
89 certainty or bias in the differential arrival time measurements made using individual seis-
90 mograms (Garnero et al., 1993) or small-aperture arrays (Eaton & Kendall, 2006). Stack-
91 ing of data from large-scale arrays (Helffrich & Kaneshima, 2010; Kaneshima & Helffrich,
92 2013; Kaneshima & Matsuzawa, 2015; Kaneshima, 2018) or global networks (Alexandrakis
93 & Eaton, 2010) tends to average out perturbations due to mantle heterogeneities and
94 therefore mitigate the possible bias. Alternatively, the bias can be evaluated using ray
95 theory (e.g. Helffrich & Kaneshima, 2010; Kaneshima & Helffrich, 2013; Kaneshima &
96 Matsuzawa, 2015; Kaneshima, 2018) or sophisticated waveform modeling (Tanaka, 2004,
97 2007), based on either known 3D mantle tomography model or hypothesized structure.
98 Combining array stacking and accurate 3D mantle corrections would be an optimal so-
99 lution to suppress 3D mantle effects, which has not been reported before.

100 To ameliorate these problems, we develop an iterative method to separate individ-
101 ual SmKS phases from the SmKS wavetrain in array data and use normalized cross-correlation
102 (CC) to measure the differential travel times between SmKS ($m=3, 4$ and 5) and SKKS.
103 We carefully select good quality data to successfully obtain each SmKS phase. The it-
104 erative method provides us with accurate waveform-based measurements of differential
105 arrival times and important information to assess the measurement quality. We use two
106 methods, ray theory and the Spectral Element Method (SEM), to investigate the effects
107 of lateral heterogeneities in the mantle, using the 3D tomography model S40RTS (Rit-
108 sema et al., 2011), and also assess the effect of choosing a different mantle model (S362ANI
109 Kustowski et al., 2008). The measured differential arrival times, after correction for 3D
110 mantle structure effects, are compared to the predictions of body-wave derived model

111 KHOMC (Kaneshima & Helffrich, 2013) and normal-mode constrained model EPOC (Irving et al., 2018).
 112

113 2 Data

114 We collected more than 320,000 seismograms from global stations from 500 earthquakes in the subduction zones of Fiji-Tonga, Vanuatu, New Britain and Solomon with
 115 depths ≥ 150 km and $M_w \geq 5.5$ (Global Centroid-Moment Tensor catalog, Ekström et al.,
 116 2012) in the period 2000-2016 (Supporting Information Fig. S1). We select events with
 117 depths ≥ 150 km to avoid contamination from depth phases sSmKS ($m \geq 2$). The seismograms have a distance range of 120 - 180° , where waveforms SmKS ($m \geq 2$) are readily
 118 observed.
 119
 120

121 We remove instrument responses and rotate the two horizontal components to get
 122 the radial displacement, on which SmKS primarily appears. Then a band-pass filter (0.05
 123 - 0.7 Hz) is applied to the data with Signal-Noise Ratio (SNR) computation. From these
 124 500 earthquakes, we find 11 events with a large number of good observations of SKKS
 125 (Fig. 2a). Here, good observation means SNR larger than 2, a large number means 100
 126 or more seismograms, and we carefully inspect the data to rule out any possible contamination from small local earthquakes. The SNR is defined as the peak-to-peak amplitude
 127 ratio of SKKS to noise. We measure SKKS amplitude in a time window between 20 s
 128 before and 50 s after the SKKS arrival time predicted by PREM (Fig. 3a). The time window of noise is taken between 70 s and 20 s before the SKKS arrival. There are total 3741
 129 radial components from these 11 events and 2535 of them have $SNR_{SKKS} > 2.0$ (Fig.
 130 2b). Limited by the geographic distribution of seismic stations, most of these clear SKKS
 131 data are from stations in Europe with a distance range of 140° - 160° and their ray paths
 132 sample the northeastern Pacific, Asia and Europe.
 133
 134

135 Following previous studies (e.g. Tanaka, 2004; Eaton & Kendall, 2006; Helffrich &
 136 Kaneshima, 2010; Alexandrakis & Eaton, 2010; Kaneshima, 2018), we use SKKS as a
 137 reference phase to investigate the arrivals of SmKS ($m > 2$), so clear SmKS ($m > 2$) signals are also important for high quality measurements. We compute SNR of SmKS ($m > 2$)
 138 and only use the data with clear SmKS ($SNR_{SmKS} \geq 2.0$, see Fig. 3). In contrast to
 139 the SNR_{SKKS} computation, we take the noise window starting after the predicted S2KS
 140 arrival time for SNR_{SmKS} (by 100 seconds) and some SmKS coda waves are included
 141

142 in this time window. Thus, the data with strong *SmKS* coda due to significant unwanted
143 source and wave propagation complexities would have low SNR_{SmKS} and therefore be
144 discarded. Then, we use the method described in section 3 to measure these data with
145 clear SmKS ($m \geq 2$). Most of our clear data are from Europe and our array-based method
146 needs a number of records to form an array, so here we focus on stations in Europe and
147 north Africa to investigate the SmKS arrivals.

148 **3 Array-based iterative method to measure SmKS-SKKS differential** 149 **arrival times**

150 **3.1 Workflow of the array-based iterative method**

151 SmKS ($m \geq 2$) series travel in the mantle and upper outer core, so their arrivals are
152 sensitive to the V_s in the mantle and V_p in the outer core. The ray paths of SKKS and
153 SmKS ($m > 2$) are close to each other in the mantle and further apart in the outer core
154 (Fig. 1a), so taking arrival time differences between SKKS and SmKS ($m > 2$), $t_{SmKS} -$
155 t_{SKKS} , instead of absolute travel time, can significantly reduce the effects of 3D V_s struc-
156 ture in the mantle and improve the constrains on the V_p in outer core. On the other hand,
157 these spatially close ray paths result in small time separations between consecutive SmKS
158 signals, which can make identifying individual SmKS phase and measuring its arrival time
159 difficult. For example, the arrival time difference between S3KS and S4KS at station ASSE
160 from event #110729 is only 13 s (Fig. 1a). The difference between S4KS and S5KS is
161 even smaller and their waveforms are mixed with each other. Many previous efforts have
162 been made to retrieve individual SmKS phase and accurately measure their arrival times
163 (e.g. Eaton & Kendall, 2006; Helffrich & Kaneshima, 2010; Kaneshima & Helffrich, 2013).
164 In particular, array stacking techniques have been used to analyze slownesses and arrival
165 times of SmKS signals (e.g. Eaton & Kendall, 2006; Helffrich & Kaneshima, 2010; Kaneshima
166 & Helffrich, 2013). Here, we take the advantage of the large number of stations with good
167 data to form one or more arrays or bins and develop an iterative method to retrieve in-
168 dividual SmKS and measure their arrival times. This iterative strategy has been used
169 to extract direct S-waves and CMB reflected ScS waves (Z. Yu et al., 2012).

170 Arrivals in the SmKS series share many factors, such as source time function, 3D
171 wave propagation effects, site responses etc., due to their similar ray paths in the crust
172 and mantle. Although their ray paths diverge further in the outer core, the outer core
173 is believed to be highly laterally homogeneous. Thus, SKKS and SmKS ($m > 2$) usually

174 have very coherent waveforms (after a $\pi(m-2)/2$ phase shift is applied to SmKS with
175 $m=3, 4$ and 5). This property helps us significantly simplify the problem and separate
176 individual SmKS waveform. In our iterative method, the reference phase SKKS is as-
177 sumed to be perfectly coherent with each SmKS ($m>2$) waveform after the phase-shift
178 is applied and only two unknown parameters, SmKS arrival time anomalies and SmKS/SKKS
179 amplitude ratios, are measured in each iteration. We note that another alternative mea-
180 suring strategy would be attempting to measure SmKS-S($m-1$)KS (i.e. S3KS-SKKS, S4KS-
181 S3KS and S5KS-S4KS), which have even closer raypaths than those of SmKS-SKKS ($m=3,$
182 4 and 5). However, this strategy suffers from the problem of weak and noisy reference
183 phases S3KS and S4KS, which would affect the performance of our method. Thus, we
184 choose the clearer SKKS waveforms as the reference phase.

185 This workflow of our iterative method is composed of data preparation and then
186 iterative measuring (Fig. 4). As described in subsection 2, we set an SNR threshold of
187 2 for both SKKS and SmKS ($m>2$) to obtain good quality data. Following (Helffrich &
188 Kaneshima, 2010; Kaneshima & Helffrich, 2013), we divide the clear SmKS data from
189 the same event into several bins and stack traces in each bin to further improve the SNR
190 (an example of one bin is shown in Fig. 5). Before stacking the traces, two steps of CC
191 are carried out on SKKS waveforms to align the data. In the first step of CC, we choose
192 one typical trace (i.e. station with the median distance of the bin) as a template (e.g.
193 black line in Fig. 5b) and compute CC of SKKS between this template and other traces
194 in this bin with shifting times. Then these traces are aligned on the time with the max-
195 imum CC values. In the next step, we stack the aligned SKKS with normalized ampli-
196 tudes to form a new template (e.g. red line in Fig. 5b) and then repeat the CC process-
197 ing to align the SmKS data again (Fig. 5c). The time window of SKKS used in CC is
198 5 s before and 30 s after the arrival time of SKKS and the maximum allowed time shift
199 is 5 s. Data with maximum CC coefficients lower than 0.8 are not used in the following
200 iterative measuring, because their low waveform similarities, due to complex site struc-
201 ture or/and instrumental issues, could decrease the quality of stacking and affect the mea-
202 surements. In these two steps of alignment, the shifted times are primarily due to 3D
203 structures near the stations, source mislocation and/or clock time errors and these fac-
204 tors are shared by SKKS and SmKS ($m>2$). Thus, shifting the traces are not expected
205 to significantly affect the measurements of differential arrival times.

206 Next, we use these aligned SmKS data to iteratively retrieve individual SmKS phases,
 207 measure differential travel time anomalies and assess quality of each measurement. In
 208 the first iteration (“*iteration1*” in Fig. 4), we stack the data in a bin and use three CC
 209 processes to measure S3KS, S4KS and S5KS one by one. For S3KS measurement, we stack
 210 S3KS using $t_{S3KS} - t_{SKKS}$ predicted by PREM (e.g. see the second red dashed line Fig.
 211 5c), apply the Hilbert transform on them to correct the 90° phase shift and then com-
 212 pute CC between stacked SKKS and S3KS to get S3KS/SKKS amplitude ratio and time
 213 delay of S3KS. Then we cut out the SKKS waveform at each station, scale them using
 214 the previously measured S3KS/SKKS amplitude ratio and apply the phase shift to get
 215 S3KS waveform estimation. This estimated S3KS is subtracted from the data to retrieve
 216 a ‘clean’ S4KS and then a similar stack-CC processing is applied on the retrieved S4KS
 217 for measurement. Once S3KS and S4KS have been measured, we can estimate both S3KS
 218 and S4KS, remove them in the data and then measure S5KS. After *iteration1*, we ob-
 219 tain initial estimations of SmKS/S2KS ($m=3, 4$ and 5) amplitude ratios and their time
 220 delays. In the next iteration, these information are used to retrieve the target SmKS and
 221 more accurately measure them. This iteration is repeated until the measurements are
 222 convergent.

223 This array-based iterative method uses good quality data and has the advantages
 224 of enhancing SNR by stacking and retrieving target SmKS signals well by removing other
 225 SmKS interfering signals. Note that we use theoretical slowness derived from PREM to
 226 stack array data, because V_p anomaly in the uppermost outer core only causes small slow-
 227 ness deviation and slowness measurements could have large uncertainties. A large slow-
 228 ness anomaly would result in less coherent stacking, which would be reflected in the CC
 229 coefficient. In the first step of data preparation, we set strict criteria to rule out the data
 230 with potential issues that might affect the validity of our method. For example, the re-
 231 quirement of $SNR_{SKKS} \geq 2.0$ allows us discard the data with high noise before SKKS.
 232 In addition to that, the other two thresholds of $SNR_{SmKS} \geq 2.0$ and $CC \geq 0.8$ rule out
 233 more bad quality data (e.g. complex SmKS waveforms and/or strong SmKS coda waves
 234 due to 3D heterogeneity or source or station structures). Stacking the data with high
 235 CC value further increases SNR and extracting individual SmKS phase from mixed sig-
 236 nals allows us reduce uncertainties in measurements. More importantly, this method pro-
 237 vides us two critical parameters to assess qualities of measurements. The most impor-
 238 tant parameter is the CC values between S2KS and target SmKS (S3KS, S4KS and S5KS).

239 A low CC value means a bad quality measurement and we should either discard it, or
240 be careful when using it. Low CC values could be due to a failure of the assumptions
241 we made, weak target signals (e.g. near the nodal plane of radiation pattern of earth-
242 quake), insufficient number of traces in a bin etc. In addition to CC values, the ampli-
243 tude information is also helpful to assess measurement quality. More details are discussed
244 in section 5.

245 Uncertainty of differential arrival time for each bin is estimated by bootstrapping
246 (Efron & Tibshirani, 1991), which reflects the variance in the bin. For each bin, we ran-
247 domly select N seismograms, with replacement, from the original N seismograms and
248 measure the differential arrival times. This process is repeated 300 times and we com-
249 pute the standard deviation of these 300 measurements as an estimation of variance in
250 that bin.

251 In next section, we demonstrate the validation of our method by testing synthetic
252 seismograms and then apply it to data.

253 3.2 Synthetic tests

254 In this subsection, we cut real SKKS waveforms from data, use them to make SmKS
255 ($m=2, 3, 4$ and 5) synthetics and then validate our iterative method. Fig. 5c shows SmKS
256 data of a bin from event #071016. We cut and taper the SKKS waveforms from 0 s to
257 40 s as input to generate S3KS, S4KS and S5KS (Fig. 6). S3KS is formed by scaling the
258 input signals with a prescribed S3KS/SKKS amplitude ratio of 0.42, applying a 90° phase
259 shift and a prescribed time shift, which is 1.13 s greater than to the PREM S3KS-SKKS
260 differential arrival time. Similarly, S4KS and S5KS are made with different amplitude
261 ratios and time delays. Then, complete SmKS synthetic seismograms are generated by
262 summing SKKS, S3KS, S4KS and S5KS.

263 Then we apply our iterative method to these synthetic seismograms and check its
264 validity. In the step of searching maximum CC values, we take a time window of 0-30
265 s after the target SmKS arrival time and the maximum allowed time shift is 5 s. In pre-
266 vious studies, the time delays of SmKS ($m=3, 4$ or 5) are less than 5 s and most of them
267 are less than 3 s (e.g. Eaton & Kendall, 2006; Helffrich & Kaneshima, 2010; Kaneshima
268 & Helffrich, 2013).

269 Fig. 7 shows the measurements from the first five iterations. We can see that both
 270 amplitude ratios and time delays are successfully retrieved and the CC values for S3KS,
 271 S4KS and S5KS are higher than 0.95 after the second iteration. In the first iteration,
 272 there are some differences between the measured results and true values. For example,
 273 the measured time delay of S4KS is ~ 2.15 s, which is ~ 0.1 s smaller than the input 2.25
 274 s. The CC value for S3KS measurement, $CC_{3,2}$, is 0.88, lower than $CC_{4,2}=0.92$ for S4KS
 275 and $CC_{4,2}=0.92$ for S5KS, because the S3KS measurement is affected by the presence
 276 of S4KS and S5KS signals. In the second iteration, the CC values are significantly in-
 277 creased and the measurements are close to the true values. The measurements become
 278 almost constant in the next three iterations, showing they reach convergence. After the
 279 first two iterations, waveforms are successfully retrieved and the time delays are accu-
 280 rately measured (e.g. see the waveform cross-correlations between SKKS and S5KS in
 281 Fig. S2). These results demonstrate the validation of our method. Of course, real data
 282 may be more complex than the synthetic SmKS here, e.g. different noise signals may be
 283 present in data, and therefore measurement quality might be not as good as in these syn-
 284 thetic tests. However, CC values indicate this complexity, demonstrating their impor-
 285 tance.

286 3.3 Correcting 3D mantle structure effects

287 Because the ray paths of SmKS ($m=2-5$) are close to each other in the mantle, many
 288 previous studies assume that the effects of 3D mantle structures are the same for SKKS
 289 and SmKS ($m>2$). Thus, the measured time delays of SmKS ($m>2$) are only due to the
 290 V_p anomalies in the top outer core. However, we know that the ray paths between SKKS
 291 and SmKS ($m>2$) are not exactly the same and the 3D mantle structures must affect
 292 the arrival time difference between SKKS and SmKS ($m>2$). Kaneshima & Matsuzawa
 293 (2015) used ray theory to investigate these mantle effects at receiver-side and source-side.
 294 At the receiver side, they found that the mantle effects on $dt_{3,2}$ are much less than 0.4 s.
 295 However, the presence of a Large Low Shear Velocity Province (LLSVP) beneath the Pa-
 296 cific could cause some time delays of SmKS ($m\geq 2$) and affect the measurements.

297 To investigate 3D mantle effects, we use two different methods, ray theory and SEM,
 298 to compute the travel time delays of SmKS and compare their differences. We use SPEC-FEM3D_globe
 299 to compute synthetic seismograms and evaluate the 3D mantle effects present in the to-
 300 mography models S4ORTS (Ritsema et al., 2011) and S362ANI (Kustowski et al., 2008).

301 As a spectral element method, the SPECFEM3D_globe package solves the weak form
302 of the seismic wave propagation equation and has the advantages of high accuracy, fast
303 computation speed, handling discontinuity topography etc. (Komatitsch & Tromp, 1999,
304 2002; Tromp et al., 2008). The adjoint source technique is part of SPECFEM3D_globe,
305 allowing the efficient computation of global scale sensitivity kernels of seismic signals in
306 a given time window and frequency band (Tromp et al., 2008; Luo et al., 2013). We set
307 the mesh parameters *NEX_XI* and *NEX_ETA* to 896 and the minimum resolved period
308 is about 4.9 s. We use source parameters from GCMT (Global Centroid Moment Ten-
309 sor, Ekström et al., 2012) and SPECFEM3D_globe to compute the synthetic seismogram
310 and the SmKS travel time sensitivity kernels. We note that GCMT solutions do not con-
311 tain detailed inversions for source duration, so we reestimate the source duration using
312 teleseismic P-waves from global stations. For comparison, we also compute the 3D man-
313 tle structure corrections based on ray theory using the S40RTS model. To simplify the
314 problem, we use PREM to get the ray path and compute the arrival time perturbations
315 along that ray path. In other words, we assume that the ray path is not dramatically
316 distorted by 3D structures.

317 Fig. 8 shows a depth cross-section of fractional velocity anomaly, dV_s/V_s , from the
318 3D model S40RTS (Ritsema et al., 2011) along the great circle connecting station GRA1
319 and event #110729. The ray paths of SmKS ($m=2, 3$ and 4) sample the LLSVP at the
320 source side, where dV_s is lower than -1% . Using this 3D V_s mantle model, we can use
321 ray theory to compute the arrival time anomalies of SmKS ($m=2, 3, 4$ and 5) along their
322 ray paths. However, ray theory only works at infinite frequency. Indeed, seismic waves
323 at a finite frequency are sensitive to a Fresnel zone, a region centered at its ray path. To
324 demonstrate the Fresnel zones of SmKS, we use the SPECFEM3D_globe package (Ko-
325 matitsch & Tromp, 1999) to compute sensitivity kernels of SmKS in the mantle and outer
326 core.

327 Fig. 8a shows the SPECFEM3D_globe synthetic seismogram at GRA1 from the
328 event #110729 and three time windows used to compute the sensitivity kernels of SKKS,
329 S3KS and S4KS. We use the GCMT solution (Ekström et al., 2012) as the input of source
330 parameters, but reestimate its source duration (Fig. S4). The S40RTS model is used to
331 describe mantle heterogeneity and attenuation simulation is disabled to speed up the com-
332 putation. We use 1536 CPU cores to run the SEM simulation, taking about 14 hours for
333 forward modeling and 27 hours for each adjoint simulation. At frequency 0.05-0.2 Hz,

334 the first Fresnel zone of SKKS (the green band centered at SKKS ray path) has a width
 335 of ~ 18 deg (~ 900 km) on the CMB and its upper boundary approaches the ray paths
 336 of S3KS and S4KS (Fig. 8). The sensitivity kernels of S3KS and S4KS have similar di-
 337 mensions (i.e. the width of the first Fresnel zone), but more complex patterns than SKKS.
 338 Compared to SKKS, S3KS and S4KS are more sensitive to the shallower outer core, re-
 339 flected in the distribution of sensitivity kernels. The wide dimensions and complex pat-
 340 terns of SmKS sensitivity kernels in Fig. 8 indicate that the 3D mantle structure cor-
 341 rections based on ray theory may cause systematic biases and uncertainties. We will dis-
 342 cuss the detailed 3D mantle structure correction of each bin and the comparison of ray
 343 theory and SEM results in subsection 4.2.

344 4 Results

345 4.1 Measuring SmKS-S2KS differential arrival times

346 We apply the iterative method to data at three frequency bands (0.05-0.2 Hz, 0.05-
 347 0.7 Hz and 0.1-0.7 Hz) and investigate the time delays of S3KS, S4KS and S5KS. For
 348 each frequency band, we compute the SNRs (SNR_{SKKS} and SNR_{SmKS}), take clear SmKS
 349 data of each event to form bins (one example of event #141101 shown in Fig. S3) and
 350 apply the iterative method to each bin.

351 We only use data at epicentral distances greater than 140° . At shorter distances,
 352 S3KS arrival times are close to SKKS (i.e. arrival time difference smaller than 27 s) and
 353 therefore might affect quality of cut SKKS waveforms. Based on the number of clear SmKS
 354 traces and the station distribution, we divide the data from each event into several ge-
 355 ographical bins. For example, the event #141101 provides more than 100 clear SmKS
 356 traces (0.05-0.2 Hz) and we divide them into four bins (see Table S1 and Fig. S3). For
 357 some bins (e.g. bin 2 from event #010526 in Table S1), the number of clear SmKS traces
 358 is too few (i.e. <10) to provide reliable measurements, so we do not use the results of
 359 these bins.

360 At frequencies 0.05-0.2 Hz, we eventually have twenty five effective bins from the
 361 eleven events (Table S1). We use the same parameters (i.e. a time window of 40 s to cut
 362 SKKS and 30 s for CC computation) as in synthetic testing and apply the iterative method
 363 to each bin. In the synthetic testing, the measured results are almost constant after the
 364 second iteration. Thus, here we conduct six iterations and take the results from the fifth

365 iteration (detailed measurements listed in Table S1). For each bin, we check the results
 366 and make sure that there is no substantial difference between the fourth and fifth and
 367 six iterations. In the twenty five bins, the measured S3KS time delay, $dt_{3,2}$, ranges from
 368 -0.03 s to 2.83 s and the S3KS/SKKS amplitude ratios, $A_{3,2}$, are between 0.35-0.71. Nine-
 369 teen bins have $CC_{3,2} \geq 0.90$ and most of the time delays are positive values, except bin
 370 1 from event #010428. S4KS and S5KS are more difficult to retrieve and measure. This
 371 is reflected in the generally lower CC values and larger measurement scatter than S3KS.
 372 Fig. 9 shows an example of bin 4 from the event #141101. All the three CC values are
 373 higher than 0.94, indicating good quality measurements. For this bin, the measured time
 374 delays are 1.30 s for S3KS, 2.48 s for S4KS and 2.59 s for S5KS. The median epicentral
 375 distance of this bin is 145.29° and those time delays would indicate a slower Vp than in
 376 PREM in the topmost outer core, consistent with previous studies (e.g. Eaton & Kendall,
 377 2006; Helffrich & Kaneshima, 2010; Kaneshima & Helffrich, 2013).

378 The measurement qualities are primarily indicated by their CC coefficients. In ad-
 379 dition to CC coefficients, amplitude information is also useful to assess the measurement
 380 quality. If other factors, such as source radiation pattern, are the same, the amplitude
 381 of the SmKS phase decreases with its order m, due to the energy loss at each reflection
 382 on the underside of the CMB. All the measurements with good quality at 0.05-0.2 Hz
 383 follow this trend of $A_{3,2} > A_{4,2} > A_{5,2}$ (amplitude information in Table S1 and the
 384 good quality measurements are listed in Tables S2,S3 and S4).

385 4.2 3D mantle structure corrections

386 We run SPECSEM3D_globe to obtain the synthetic seismograms corresponding to
 387 the data with good quality measurements. Here, good quality means that more than ten
 388 traces are used in a bin and $CC_{3,2} \geq 0.90$ (Table S1). Most source parameters used in
 389 the SEM simulations are from GCMT, but the source durations are replaced with our
 390 estimated values. Then we apply our iterative method to these synthetic seismograms
 391 to obtain the time delays, amplitude ratios and corresponding CC values. For most bins,
 392 we successfully retrieve signals of S3KS, S4KS and S5KS and get high CC coefficients
 393 (Table S2). For example, Fig. S5 shows the measurements using synthetic seismograms
 394 corresponding to the bin 4 from the event #141101. The CC coefficients are 0.95 for S3KS,
 395 0.96 for S4KS and 0.94 for S5KS, indicating good measurement quality. The S3KS time
 396 delay, $3dM_{3,2}^{SEM}$, is as large as 0.60 s and the S4KS time delay, $dt_{4,2}^{SEM}$, is even larger,

397 1.13 s. The time delays measured on the data are 1.30 s for S3KS and 2.48 s for S4KS
 398 (Table S1). Thus, 3D mantle structure corrections are large, up to nearly half the size
 399 of the observations, and can not be ignored for this bin. The S3KS measurements on syn-
 400 thetic seismograms of other bins are listed in Table S2 and almost all the bins have $CC_{3,2}^{SEM}$
 401 higher than 0.95, except the bin 1 from #010428 and bin 1 from #140721. The S3KS/SKKS
 402 amplitude ratios range from 0.30 to 0.51 and the corrections to S3KS time delays are be-
 403 tween -0.95 s and 0.04 s. Most of the corrections have negative values, indicating that
 404 S3KS are delayed more than SKKS by the 3D mantle structure. The results for S4KS
 405 and S5KS are listed in Tables S3 and S4.

406 We also use ray theory to compute 3D mantle structure corrections for data at in-
 407 dividual stations in each bin and take the average value to represent the correction for
 408 that bin. These corrections are close to that measured on SEM synthetic seismograms
 409 (Tables S2, S3, S4 and Fig. S6). However, large discrepancies are present for some bins.
 410 For example, the correction to S3KS time delay based on ray theory is 0.27 s for the bin
 411 5 from #141101, but it is -0.22 s using SEM synthetic seismograms.

412 Fig. 10 shows the SmKS ($m=3, 4$ and 5) time delays measured on the data with
 413 high CC coefficients and the results after 3D mantle structure corrections. Here, we re-
 414 quire $CC_{3,2} \geq 0.90$ for a good quality of S3KS measurement. For S4KS, we only take
 415 the bins with $CC_{4,2} \geq 0.85$ and $CC_{3,2} \geq 0.90$, because a good quality of S4KS measure-
 416 ment relies on a well-retrieved S3KS. Similarly, we require $CC_{3,2} \geq 0.90$, $CC_{4,2} \geq 0.85$
 417 and $CC_{5,2} \geq 0.80$ for good quality of S5KS measurements.

418 Most of the bins with good qualities of $dt_{3,2}$ measurements have uncertainties smaller
 419 than 0.4 s (Table S2). It is not surprising that $dt_{4,2}$ and $dt_{5,2}$ generally show larger un-
 420 certainties than $dt_{3,2}$, due to their smaller SNR and/or incomplete separation of SmKS
 421 ($m=2, 3, 4$ and 5) waveforms of our method. In spite of this, the uncertainties are still
 422 much smaller than the anomalies (Tables S4 and S5), because the bins with large errors,
 423 resulted from poor phase stripping and/or low SNRs, are discarded by the CC require-
 424 ments. We note that bootstrapping results only help us infer variance in the dataset, but
 425 not able to estimate systematic bias. The systematic bias could be due to strong man-
 426 tle heterogeneities and source complexities etc, which can be assessed by investigating
 427 global data from earthquakes at various places.

4.3 Comparison between observations and predictions of two 1D models, EPOC and KHOMC

From Fig. 10, we can see that S3KS, S4KS and S5KS time delays predicted by EPOC (Irving et al., 2018) and KHOMC (Kaneshima & Helffrich, 2013) are close to each other at distance 140° – 155° , where most of our data are located. The measured S3KS time delays are generally positive and consistent with the KHOMC and EPOC predictions supporting a slower V_p in the top outer core. The 3D mantle structure corrections, using either ray theory or SEM synthetic seismograms, are primarily negative and therefore reduce the measured S3KS time delays. After the corrections, travel time anomalies are less than the EPOC predictions and they seem to fit the KHOMC predictions better than that of EPOC. The difference between these two models can be better resolved using data at distances $> 160^\circ$, where their difference is larger than 0.5 s. Unfortunately, we have only one such datum, at a distance of 167.8° , so we can not clearly distinguish between EPOC and KHOMC. For S4KS and S5KS, the 3D mantle structure corrections are also primarily negative and they make measurements closer to the KHOMC and EPOC predictions. However, there are a few measurements dramatically departing from the EPOC and KHOMC predictions. For example, $dt_{4,2}^{SEM}$ of bin 1 from #140721 is -0.22 s while the EPOC prediction is 1.22 s. For this bin, the two types of 3D mantle structure corrections have a large difference, 0.12 s from ray theory computation and -0.95 s from SEM synthetic seismograms. This large difference could be due to the limitation of ray theory, uncertainty in the S40RTS model, or poor performance of our method on the synthetic seismograms of this bin. The $CC_{3,2}^{SEM}$ is only 0.91, much lower than that of other bins, which indicates a poor measurement quality. However, $CC_{3,2}$ from data is a high value of 0.96 and its $dt_{3,2}^{ray}$ is close to the EPOC and KHOMC predictions. This big difference is most likely due to a large uncertainty in the 3D mantle corrections using SEM synthetic seismograms. Some other bins, including S3KS time delays of bin 1 from #010428 and S5KS time delays of bin 1 from #010516, have similar issues. Note that the S5KS time delay of bin 1 from #010516 is beyond the y-axis range and not plotted in Fig. 10c.

We also apply two other filters, 0.05-0.7 Hz and 0.1-0.7 Hz, to the data and repeat the measurements. Because running SPEC-FEM3D-globe to resolve a frequency of 0.7 Hz is very computationally expensive, we only compute the 3D mantle structure corrections using ray theory. Similar to the results at 0.05-0.2 Hz, the S3KS, S4KS and S5KS

461 measurements at 0.05-0.7 Hz are close to the EPOC and KHMOC predictions after the
462 3D mantle structure corrections (see Fig. S7).

463 Note that the bins shown in Fig. S7 are not the same as 0.05-0.7 Hz, because the
464 SNRs of data may change with frequency band and the measurement qualities could also
465 be different. Comparing to 0.05-0.2 Hz and 0.05-0.7 Hz, the number of bins with good
466 measurement qualities is lower at 0.1-0.7 Hz, indicating lower SNRs of data and/or re-
467 duced performance of our iterative method for this high frequency band for the data used
468 here. Relatively long period SmKS waves have been stacked to investigate outermost core
469 structure (e.g. 0.02-0.1 Hz in Tanaka, 2007). Shorter period waves have the potential
470 to resolve finer seismic structure. However, source rupture processes and propagation
471 effects due to lateral heterogeneities could give rise to more waveform complexities at
472 shorter period waves reducing the waveform coherencies of SmKS phases and therefore
473 affecting measurement qualities. This might explain the lower number of good quality
474 measurements (Figs. S7d-f) at 0.1-0.7 Hz than that at 0.05-0.2 Hz (Fig. 10) and 0.05-
475 0.7 Hz (Figs. S7a-c).

476 5 Discussion

477 SmKS differential arrival times are sensitive to the outer core structure, but accu-
478 rate measurements of differential arrival times are hampered by their mixed waveforms
479 as a whispering-gallery mode. To extract each individual SmKS phase, Eaton & Kendall
480 (2006) use SKKS as reference waveform and apply deconvolution to SmKS series to con-
481 vert their waveforms into simple pulses. However, the deconvolution method either re-
482 quires very high SNR and or has reduced resolution. Here, we develop an iterative method
483 to isolate individual SmKS waveforms with a high resolution. Our method keeps wave-
484 form features of each SmKS and therefore allows us to measure SmKS time delays by
485 CC.

486 We use two different methods, ray theory and SEM synthetic seismograms, to com-
487 pute effects of mantle heterogeneities and make these corrections to the measurements.
488 The corrections are between -0.5 s and 0.5 s for most bins, but some bins have 3D man-
489 tle perturbations even greater than 1.0 s. Furthermore, we see big differences between
490 the two types of corrections for some data (e.g. > 1 s for bin 1 from event #140721),
491 although they generally have positive correlation (Fig. S6). We also used another 3D man-

492 the model S362ANI (Kustowski et al., 2008) to compute the SEM synthetic seismograms
493 and measure the 3D mantle structure corrections. Compared to our results using S40RTS,
494 the corrections to S3KS-SKKS, S4KS-SKKS and S5KS-SKKS differential arrival times
495 using S362ANI are generally stronger. Consequently, the corrected SmKS-SKKS ($m=3$,
496 4 and 5) time delays become even smaller (Fig. S8,9). Helffrich & Kaneshima (2013) used
497 earthquakes in Fiji and Argentina to investigate SmKS-SKKS time delays. Their mea-
498 sured S3KS-SKKS time delays from Fiji are generally larger than that from Argentina.
499 The earthquakes in our study are geographically close to Fiji and the 3D mantle correc-
500 tions to S3KS-SKKS time delays tend to reduce the S3KS-SKKS time delays (Fig. 10a).
501 Thus, the higher S3KS-SKKS time delays from events in Fiji by (Helffrich & Kaneshima,
502 2013) can be largely explained with the 3D mantle structure. 3D mantle structure cor-
503 rections should be routinely considered to reduce bias in the V_p estimation of uppermost
504 outer core.

505 After correcting for 3D mantle structure, there are still significant SmKS-SKKS time
506 delays at all of the three frequency bands (Figs. 10 and S7), indicating a lower V_p than
507 PREM model in the shallow outer core. Strong locally concentrated heterogeneities, such
508 as the previously detected Ultra Low Velocity Zones (ULVZs) at the source side of our
509 study region (see, for example, the compilations by S. Yu & Garnero, 2018), are not ac-
510 curately represented in the smooth global tomography model of S40RTS and could af-
511 fect the measurements. However, these ULVZ effects have been investigated by Tanaka
512 (2007) and they are expected to be smaller than our measured time delays. In addition,
513 such strong heterogeneities would decrease the coherencies between SKKS and SmKS
514 ($m=3$, 4 and 5) and only the results with high CC values are selected in our method. Fur-
515 ther quantitative investigations will rely on better constraints on the properties and ge-
516 ographical distributions of ULVZ and more detailed numerical waveform modeling. Thus,
517 we do not believe that the SmKS-SKKS travel time delays are solely due to ULVZs, but
518 do indeed indicate a seismically slow uppermost outer core.

519 Although scatter and uncertainty are present, our measurements are generally con-
520 sistent with the predictions by the KHOMC and EPOC models. Assuming the outer core
521 is homogeneous, Irving et al. (2018) use a physically consistent equation-of-state (EoS)
522 to parameterize the elastic properties of outer and carry out inversions for seismic nor-
523 mal mode data. This normal mode derived EPOC model shows lower V_p and higher den-
524 sity than PREM at the top of outer core. Although EPOC does not use body-wave data,

525 its fit to SmKS data is better than PREM (see Fig. 3 in Irving et al. (2018) and Figs.
526 10 and S7 in this study). KHOMC is derived from SmKS body-wave travel time anoma-
527 lies and has higher depth resolution than EPOC. We note that both EPOC and KHOMC
528 models have a low V_p at the top of outer core, but they have different depth gradients
529 of V_p . KHOMC seems to fit our results better than EPOC. For example, EPOC over-
530 predicts most S3KS-SKKS time delays after 3D mantle corrections. However, given the
531 scatter present in our measurements, either EPOC or KHOMC fits the data well. The
532 contrast between stratified or homogeneous structure has important implications for un-
533 derstanding the thermochemical status of core and the associated geodynamo. A strat-
534 ified outer core would change the flow in the outer core and therefore affect the secular
535 variation of geomagnetic field (e.g. Braginsky, 1993; Buffett, 2014; Buffett et al., 2016).
536 However, the detailed effects of such stratification on the geodynamo and the compat-
537 ibility between seismic and geomagnetic observations (e.g. the thickness of stratified layer)
538 are still inconclusive (Gubbins, 2007; Buffett, 2014; Chulliat & Maus, 2014; Lesur et al.,
539 2015). Additionally, the mechanism for the formation of stratification is also under de-
540 bate. For example, high concentrations of light elements, including S, O, Si, C and H,
541 at the top of outer core could cause a stratification (e.g. Fearn & Loper, 1981; Buffett
542 & Seagle, 2010; Gubbins & Davies, 2013; Nakagawa, 2018; Helffrich & Kaneshima, 2013),
543 but how these light elements change V_p is still under debate (Helffrich, 2012; Brodholt
544 & Badro, 2017). In this study, we cannot easily distinguish between the EPOC and KHOMC
545 models, but these two models do give different predictions of SmKS-SKKS differential
546 arrival times. Thus, both gathering more observations, e.g. S3KS-SKKS differential times
547 at a distance $> 160^\circ$, and considering other geophysical probes of the outer core, for ex-
548 ample normal mode observations, will be critical to better resolve the uppermost outer
549 core's density and V_p , providing vital data to constrain the thermochemical status of
550 the outer core.

551 **6 Conclusions**

552 We introduce an array-based iterative method to measure SmKS-SKKS ($m=3, 4$
553 and 5) differential arrival times and use them to investigate the V_p in Earth's uppermost
554 outer core. We validate this method by testing synthetic seismograms and apply this method
555 to data at stations in Europe from eleven earthquakes in Fiji-Tonga, Vanuatu, New Britain
556 and Solomon Islands. Using the SKKS signal as a reference, S3KS, S4KS and S5KS wave-

557 forms are successfully extracted and S3KS-SKKS, S4KS-SKKS and S5KS-SKKS differ-
558 ential arrival times are measured by waveform cross-correlation. This iterative method
559 not only gives us the measurements of differential arrival times, but also allow us to as-
560 sess measurement qualities based the CC coefficients and amplitude information. SmKS-
561 SKKS differential arrival times are sensitive to V_p at the top of the outer core, but 3D
562 mantle structures could also affect the arrival times. We use the 3D mantle model S40RTS
563 and two different methods, ray theory and SEM synthetic seismograms, to estimate these
564 anomalies for the frequency of 0.05-0.2 Hz. The results show that the arrival time anoma-
565 lies due to 3D mantle structure effects are large (e.g. > 0.5 s) for some data and some-
566 times there are big differences between the corrections calculated using ray theory and
567 SEM synthetics. After corrections for 3D mantle structure, we still see large positive S3KS-
568 SKKS, S4KS-SKKS and S5KS-SKKS differential arrival times, indicating a lower V_p than
569 in PREM at the top of outer core. Our measurements are consistent with the predic-
570 tions of KHOMC and EPOC models. EPOC has a homogeneous outer core while KHOMC
571 contains a stratified layer at the top of outer core. Based on the data in this study, we
572 cannot clearly distinguish the KHOMC and EPOC models, so more data, e.g. S3KS-SKKS
573 differential time at a distances $> 160^\circ$, will be necessary to help us distinguish between
574 them.

575 Acknowledgments

576 We acknowledge support from the NSF (EAR1644399 and 1736046). The authors
577 thank J. Ristema and C.A. Moreno Chaves for their code to calculate ray theoretical times
578 through S40RTS. The authors acknowledge the use of the GMT (Wessel & Smith, 1998)
579 and SAC (Goldstein et al., 2003) software packages. We acknowledge support from the
580 NSF (EAR1644399 and 1736046). Waveform data (from a range of networks detailed in
581 the References) have been collected using the Python toolbox ObsPy (Beyreuther et al.,
582 2010).

583 References

- 584 Alexandrakis, C., & Eaton, D. W. (2007). Empirical transfer functions: Application
585 to determination of outermost core velocity structure using SmKS phases. *Geo-*
586 *phys. Res. Lett.*, *34*, L22317. doi: 10.1029/2007gl031932
- 587 Alexandrakis, C., & Eaton, D. W. (2010). Precise seismic-wave velocity atop Earth's

- 588 core: No evidence for outer-core stratification. *Phys. Earth Planet. Inter.*, 180(1-
589 2), 59–65. doi: 10.1016/j.pepi.2010.02.011
- 590 Beyreuther, M., Barsch, R., Krischer, L., Megies, T., Behr, Y., & Wassermann, J.
591 (2010). ObsPy: A Python Toolbox for Seismology. *Seismol. Res. Lett.*, 81(3),
592 530–533. doi: 10.1785/gssrl.81.3.530
- 593 Braginsky, S. I. (1993). MAC-Oscillations of the Hidden Ocean of the Core. *J. Geo-
594 magn. Geoelectr.*, 45(11), 1517–1538. doi: 10.5636/jgg.45.1517
- 595 Brodholt, J., & Badro, J. (2017). Composition of the low seismic velocity E' layer
596 at the top of Earth's core. *Geophys. Res. Lett.*, 44(16), 8303–8310. doi: 10.1002/
597 2017GL074261
- 598 Buffett, B. (2014). Geomagnetic fluctuations reveal stable stratification at the top of
599 the Earth's core. *Nature*, 507(7493), 484–487. doi: 10.1038/nature13122
- 600 Buffett, B., Knezek, N., & Holme, R. (2016). Evidence for MAC waves at the top
601 of Earth's core and implications for variations in length of day. *Geophys. J. Int.*,
602 204(3), 1789–1800. doi: 10.1093/gji/ggv552
- 603 Buffett, B., & Seagle, C. (2010). Stratification of the top of the core due to chem-
604 ical interactions with the mantle. *J. Geophys. Res.*, 115, B04407. doi: 10.1029/
605 2009jb006751
- 606 Choy, G. L. (1977). Theoretical seismograms of core phases calculated by frequency-
607 dependent full wave theory, and their interpretation. *Geophys. J. Int.*, 51(2), 275–
608 312. doi: 10.1111/j.1365-246x.1977.tb06921.x
- 609 Choy, G. L., & Richards, P. G. (1975). Pulse distortion and hilbert transformation
610 in multiply reflected and refracted body waves. *Bull. Seismol. Soc. Am.*, 65(1),
611 55–70.
- 612 Chulliat, A., & Maus, S. (2014). Geomagnetic secular acceleration, jerks, and a
613 localized standing wave at the core surface from 2000 to 2010. *J. Geophys. Res.*,
614 119(3), 1531–1543. doi: 10.1002/2013JB010604
- 615 Dziewonski, A. M., & Anderson, D. L. (1981). Preliminary reference Earth model.
616 *Phys. Earth Planet. Inter.*, 25(4), 297–356. doi: 10.1016/0031-9201(81)90046-7
- 617 Eaton, D. W., & Kendall, J.-M. (2006). Improving seismic resolution of out-
618 ermost core structure by multichannel analysis and deconvolution of broad-
619 band SmKS phases. *Phys. Earth Planet. Inter.*, 155(1-2), 104–119. doi:
620 10.1016/j.pepi.2005.10.007

- 621 Efron, B., & Tibshirani, R. (1991, jul). Statistical Data Analysis in the Computer
622 Age. *Science*, *253*(5018), 390–395. doi: 10.1126/science.253.5018.390
- 623 Ekström, G., Nettles, M., & Dziewoński, A. (2012). The global CMT project
624 2004–2010: Centroid-moment tensors for 13,017 earthquakes. *Phys. Earth
625 Planet. Inter.*, *200-201*, 1–9. doi: 10.1016/j.pepi.2012.04.002
- 626 Fearn, D. R., & Loper, D. E. (1981). Compositional convection and stratification of
627 Earth’s core. *Nature*, *289*(5796), 393. doi: 10.1038/289393a0
- 628 Garnero, E. J., & Helmberger, D. V. (1995). On seismic resolution of lateral hetero-
629 geneity in the Earth’s outermost core. *Phys. Earth Planet. Inter.*, *88*(2), 117–130.
630 doi: 10.1016/0031-9201(94)02976-i
- 631 Garnero, E. J., Helmberger, D. V., & Engen, G. (1988). Lateral variations near
632 the core-mantle boundary. *Geophys. Res. Lett.*, *15*(6), 609–612. doi: 10.1029/
633 gl015i006p00609
- 634 Garnero, E. J., Helmberger, D. V., & Grand, S. P. (1993). Constraining outermost
635 core velocity with SmKS waves. *Geophys. Res. Lett.*, *20*(22), 2463–2466. doi: 10
636 .1029/93gl02823
- 637 Garnero, E. J., McNamara, A. K., & Shim, S.-H. (2016). Continent-sized anomalous
638 zones with low seismic velocity at the base of Earth’s mantle. *Nat. Geosci.*, *9*(7),
639 481–489. doi: 10.1038/ngeo2733
- 640 Goldstein, P., Dodge, D., Firpo, M., & Minner, L. (2003). SAC2000: Signal process-
641 ing and analysis tools for seismologists and engineers. *The IASPEI International
642 Handbook of Earthquake and Engineering Seismology*, *81*, 1613–1620.
- 643 Gubbins, D. (2007). Geomagnetic constraints on stratification at the top of Earth’s
644 core. *Earth Planets Space*, *59*(7), 661–664. doi: 10.1186/bf03352728
- 645 Gubbins, D., & Davies, C. (2013). The stratified layer at the core-mantle boundary
646 caused by barodiffusion of oxygen, sulphur and silicon. *Phys. Earth Planet. Inter.*,
647 *215*, 21–28. doi: 10.1016/j.pepi.2012.11.001
- 648 Hales, A., & Roberts, J. (1971). The velocities in the outer core. *Bull. Seis-
649 mol. Soc. Am.*, *61*(4), 1051–1059.
- 650 Helffrich, G. (2012). How light element addition can lower core liquid wave speeds.
651 *Geophys. J. Int.*, *188*(3), 1065–1070. doi: 10.1111/j.1365-246x.2011.05295.x
- 652 Helffrich, G., & Kaneshima, S. (2010). Outer-core compositional stratification from
653 observed core wave speed profiles. *Nature*, *468*(7325), 807–810. doi: 10.1038/

654 nature09636

655 Helffrich, G., & Kaneshima, S. (2013). Causes and consequences of outer core strati-
656 fication. *Phys. Earth Planet. Inter.*, *223*, 2–7. doi: 10.1016/j.pepi.2013.07.005

657 Hirose, K., Labrosse, S., & Hernlund, J. (2013). Composition and state of the core.
658 *Annu. Rev. Earth Planet. Sci.*, *41*, 657–691. doi: 10.1146/annurev-earth-050212
659 -124007

660 Irving, J. C. E., Cottaar, S., & Lekić, V. (2018). Seismically determined elastic pa-
661 rameters for Earth’s outer core. *Sci. Adv.*, *4*(6), eaar2538. doi: 10.1126/sciadv
662 .aar2538

663 Kaneshima, S. (2018). Array analyses of SmKS waves and the stratification
664 of earth’s outermost core. *Phys. Earth Planet. Inter.*, *276*, 234–246. doi:
665 10.1016/j.pepi.2017.03.006

666 Kaneshima, S., & Helffrich, G. (2013). V_p structure of the outermost core derived
667 from analysing large-scale array data of SmKS waves. *Geophys. J. Int.*, *193*(3),
668 1537–1555. doi: 10.1093/gji/ggt042

669 Kaneshima, S., & Matsuzawa, T. (2015). Stratification of Earth’s outermost core in-
670 ferred from SmKS array data. *Prog Earth Planet Sci*, *2*(1). doi: 10.1186/s40645
671 -015-0046-5

672 Komatitsch, D., & Tromp, J. (1999). Introduction to the spectral element method
673 for three-dimensional seismic wave propagation. *Geophys. J. Int.*, *139*(3), 806–822.
674 doi: 10.1046/j.1365-246x.1999.00967.x

675 Komatitsch, D., & Tromp, J. (2002). Spectral-element simulations of global seis-
676 mic wave propagation-II. three-dimensional models, oceans, rotation and self-
677 gravitation. *Geophys. J. Int.*, *150*(1), 303–318. doi: 10.1046/j.1365-246x.2002
678 .01716.x

679 Kustowski, B., Ekström, G., & Dziewoński, A. (2008). Anisotropic shear-wave ve-
680 locity structure of the Earth’s mantle: A global model. *J. Geophys. Res.*, *113*(B6).
681 doi: 10.1029/2007jb005169

682 Lesur, V., Whaler, K., & Wardinski, I. (2015). Are geomagnetic data consistent with
683 stably stratified flow at the core-mantle boundary? *Geophys. J. Int.*, *201*(2), 929–
684 946. doi: 10.1093/gji/ggv031

685 Luo, Y., Tromp, J., Denel, B., & Calandra, H. (2013). 3D coupled acoustic-elastic
686 migration with topography and bathymetry based on spectral-element and adjoint

- 687 methods. *Geophysics*, 78(4), S193–S202. doi: 10.1190/geo2012-0462.1
- 688 Nakagawa, T. (2018). On the thermo-chemical origin of the stratified region at the
689 top of the Earth’s core. *Phys. Earth Planet. Inter.*, 276, 172–181. doi: 10.1016/j
690 .pepi.2017.05.011
- 691 Ohtaki, T., & Kaneshima, S. (2015). Independent estimate of velocity structure of
692 Earth’s lowermost outer core beneath the northeast Pacific from PKiKP- PKPbc
693 differential traveltimes and dispersion in PKPbc. *J. Geophys. Res.*, 120(11), 7572–
694 7586. doi: 10.1002/2015jb012140
- 695 Ritsema, J., Deuss, A., van Heijst, H. J., & Woodhouse, J. H. (2011). S40RTS:
696 a degree-40 shear-velocity model for the mantle from new Rayleigh wave disper-
697 sion, teleseismic traveltimes and normal-mode splitting function measurements.
698 *Geophys. J. Int.*, 184(3), 1223–1236. doi: 10.1111/j.1365-246x.2010.04884.x
- 699 Song, X., & Helmberger, D. V. (1995). A P-wave velocity model of Earth’s core.
700 *J. Geophys. Res.*, 100(B6), 9817–9830. doi: 10.1029/94JB03135
- 701 Souriau, A., & Poupinet, G. (1991a). A study of the outermost liquid core using dif-
702 ferential travel times of the SKS, SKKS and S3KS phases. *Phys. Earth Planet. In-
703 ter.*, 68(1-2), 183–199. doi: 10.1016/0031-9201(91)90017-c
- 704 Souriau, A., & Poupinet, G. (1991b). The velocity profile at the base of the liquid
705 core from PKP(BC+Cdiff) data: An argument in favour of radial inhomogeneity.
706 *Geophys. Res. Lett.*, 18(11), 2023–2026. doi: 10.1029/91gl02417
- 707 Stevenson, D. (1987). Limits on lateral density and velocity variations in
708 the Earth’s outer core. *Geophys. J. Int.*, 88(1), 311–319. doi: 10.1111/
709 j.1365-246x.1987.tb01383.x
- 710 Tanaka, S. (2004). Seismic detectability of anomalous structure at the top of the
711 Earth’s outer core with broadband array analysis of SmKS phases. *Phys. Earth
712 Planet. Inter.*, 141(3), 141–152. doi: 10.1016/j.pepi.2003.11.006
- 713 Tanaka, S. (2007). Possibility of a low P-wave velocity layer in the outermost core
714 from global SmKS waveforms. *Earth Planet. Sci. Lett.*, 259(3-4), 486–499. doi: 10
715 .1016/j.epsl.2007.05.007
- 716 Tang, V., Zhao, L., & Hung, S.-H. (2015). Seismological evidence for a non-
717 monotonic velocity gradient in the topmost outer core. *Scientific Reports*, 5(1),
718 8613. doi: 10.1038/srep08613
- 719 Tromp, J., Komatitsch, D., & Liu, Q. (2008). Spectral-element and adjoint methods

720 in seismology. *Comm. Comput. Phys.*, 3(1), 1–32.

721 The waveform data used in this study is from the following networks:

722 AC, AF (doi:10.7914/SN/AF), BA, BE (doi:10.7914/SN/BE), BL,
 723 BN, BS (doi:10.7914/SN/BS), BW (doi:10.7914/SN/BW), C, C1
 724 (doi:10.7914/SN/C1), CA (doi:10.7914/SN/CA), CB (doi:10.7914/SN/CB),
 725 CH (doi:10.12686/sed/networks/ch), CM, CN (doi:10.7914/SN/CN),
 726 CR, CU (doi:10.7914/SN/CU), CX (doi:10.14470/PK615318), CZ
 727 (doi:10.7914/SN/CZ), DK, DR (doi:10.7914/SN/DR), DZ, EB,
 728 EE, EI (doi:10.7914/SN/EI), FN, FR (doi:10.15778/RESIF.FR), G
 729 (doi:10.18715/GEOSCOPE.G), GB, GE (doi:10.14470/TR560404), GR, GS
 730 (doi:10.7914/SN/GS), GT (doi:10.7914/SN/GT), GU (doi:10.7914/SN/GU),
 731 HE (doi:10.14470/UR044600), HL (doi:10.7914/SN/HL), HT
 732 (doi:10.7914/SN/HT), HU (doi:10.14470/UH028726), IB (doi:10.7914/SN/IB),
 733 II(doi:10.7914/SN/II), IM, IP, IS, IU(doi:10.7914/SN/IU), IV
 734 (doi:10.13127/SD/X0FXnH7QfY), KC (doi:10.7914/SN/KC), KN, KO
 735 (doi:10.7914/SN/KO), KP (doi:10.7914/SN/KP), KR (doi:10.7914/SN/KR),
 736 KW, KZ (doi:10.7914/SN/KZ), LD, LI (doi:10.7914/SN/LI), LX,
 737 MC, MD (doi:10.7914/SN/MD), MN (doi:10.13127/SD/fBBBtDtd6q),
 738 MX (doi:10.21766/SSNMX/SN/MX), N₄ (doi:10.7914/SN/N₄), NA
 739 (doi:10.21944/dffa7a3f-7e3a-3b33-a436-516a01b6af3f), NE (doi:10.7914/SN/NE),
 740 NI (doi:10.7914/SN/NI), NJ (doi:10.7914/SN/NJ), NL (doi:10.21944/e970fd34-
 741 23b9-3411-b366-e4f72877d2c5), NM, NO, NR (doi:10.7914/SN/NR), NU
 742 (doi:10.7914/SN/NU), OE (doi:10.7914/SN/OE), OV, OX (doi:10.7914/SN/OX),
 743 PE (doi:10.7914/SN/PE), PL, PM, PR (doi:10.7914/SN/PR), PZ
 744 (doi:10.7914/SN/PZ), RD (doi:10.15778/RESIF.RD), RO (doi:10.7914/SN/RO),
 745 SI, SJ, SK (doi:10.14470/FX099882), SL (doi:10.7914/SN/SL),
 746 SP (doi:10.7914/SN/SP), SS, SV, SX (doi:10.7914/SN/SX), TA
 747 (doi:10.7914/SN/TA), TH (doi:10.7914/SN/TH), TR, TT, TU, UK,
 748 UP (doi:10.18159/SNSN), US (doi:10.7914/SN/US), VE, VI, WC, WI
 749 (doi: doi:10.18715/antilles.WI), WM (doi:10.14470/JZ581150), X5,
 750 X6 (doi:10.7914/SN/X6_2007), X7 (doi:10.15778/RESIF.X72010),
 751 XB (doi:10.7914/SN/XB_2009), XE (doi:10.7914/SN/XE_2009), XI
 752 (doi:10.7914/SN/XI_2011), XJ (doi:10.12686/sed/networks/xh), XK

753 (doi:10.7914/SN/XK_2012), XN (doi:10.7914/SN/XN_2008), XO
 754 (doi:10.7914/SN/XO_2011), XQ (doi:10.7914/SN/XQ_2012), XT
 755 (doi:10.7914/SN/XT_2003), XV (doi:10.7914/SN/XV_2011), XW
 756 (doi:10.15778/RESIF.XW2007 and doi:10.7914/SN/XW_2009), XY
 757 (doi:10.15778/RESIF.XY2007 and doi:10.7914/SN/XY_2010), XZ
 758 (doi:10.7914/SN/XZ_2003), Y1, Y4 (doi:10.15778/RESIF.Y42004), YB
 759 (doi:10.15778/RESIF.YB2000 and doi:10.7914/SN/YB_2013), YD, YF,
 760 YG, YH (doi:10.7914/SN/YH_2012), YI (doi:10.7914/SN/YI_2003 and
 761 doi:10.15778/RESIF.YI2008), YJ, YK, YO (doi:10.7914/SN/YO_2014), YP,
 762 YQ (doi:10.7914/SN/YQ_2013), YR (doi:10.15778/RESIF.YR1999), YS
 763 (doi:10.7914/SN/YS_2009), YV, YW, YY, YZ (doi:10.7914/SN/YZ_2009),
 764 Z4 (doi:10.7914/SN/Z4_2009), Z9 (doi:10.7914/SN/Z9_2010), ZA,
 765 ZC (doi:10.7914/SN/ZC_2013), ZD (doi:10.7914/SN/ZD_2010), ZE
 766 (doi:10.7914/SN/ZE_2007), ZF, ZG (doi:10.7914/SN/ZG_2010), ZH
 767 (doi:10.15778/RESIF.ZH2003), ZL (doi:10.7914/SN/ZL_2007), ZN, ZO
 768 (doi:10.7914/SN/ZO_2010), ZP, ZR, ZS, ZT (doi:10.7914/SN/ZT_2015),
 769 ZU, ZV, ZX, ZZ (doi:10.14470/MM7557265463), 1E, 4F, 6D, 6E, 7A
 770 (doi:10.7914/SN/7A_2013), 7C (doi:10.15778/RESIF.7C2009), 7E
 771 (doi:10.14470/2R383989), 7J, 8A, 9D (doi:10.7914/SN/9A_2012). (n.d.).
 772 Wessel, P., & Smith, W. H. (1998). New, improved version of Generic Mapping
 773 Tools released. *EOS Trans. Amer. Geophys. Union*, 79(47), 579–579. doi: 10
 774 .1029/98EO00426
 775 Yu, S., & Garnero, E. J. (2018). Ultralow Velocity Zone Locations: A Global Assess-
 776 ment. *Geochem. Geophys. Geosyst.*, 19(2), 396–414. doi: 10.1002/2017gc007281
 777 Yu, Z., Ni, S., Wei, S., Zeng, X., Wu, W., & Li, Z. (2012). An iterative algorithm for
 778 separation of S and ScS waves of great earthquakes. *Geophys. J. Int.*, 191(2), 591–
 779 600. doi: 10.1111/j.1365-246x.2012.05603.x
 780 Zou, Z., Koper, K. D., & Cormier, V. F. (2008). The structure of the base of the
 781 outer core inferred from seismic waves diffracted around the inner core. *J. Geo-
 782 phys. Res.*, 113(B5). doi: 10.1029/2007jb005316

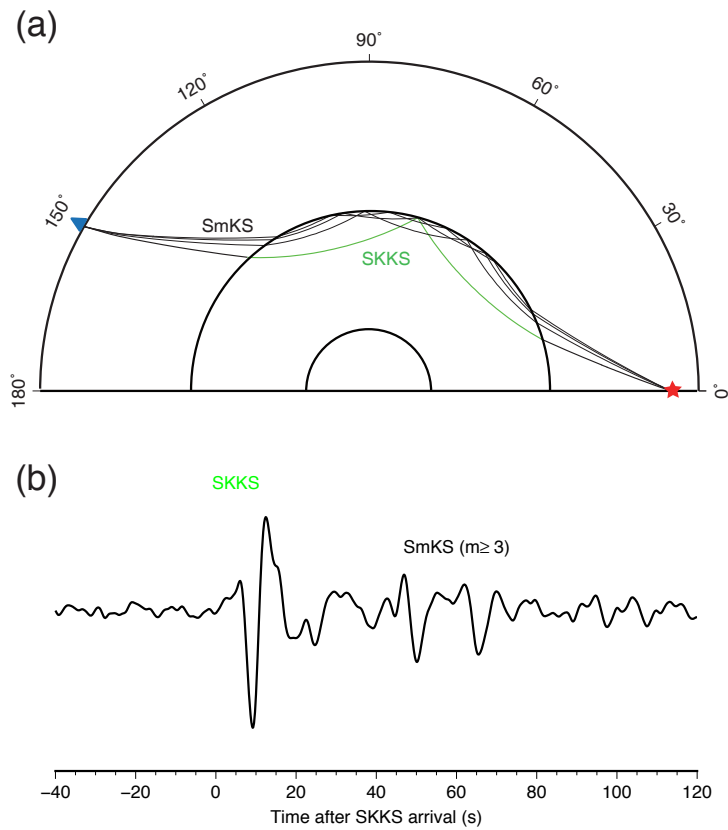


Figure 1: Ray paths of SmKS waves and one example of SmKS waveforms. (a) Ray paths of SmKS. The red star is an earthquake and the blue triangle represents a seismic station. The green line shows the ray path of SKKS traveling in the outer core. The black lines are ray paths of SmKS ($m=3, 4$ and 5) and sections of SKKS ray path traveling in the mantle and crust. (b) A band-pass filtered (bp 0.05-0.7 Hz) seismogram of SmKS data from station ASSE with an epicentral distance of 150.5° from the event #110729 (Table S1). Time zero is the SKKS arrival predicted by PREM. The predicted arrival time of S3KS is 39 s after SKKS. S4KS arrives at 52 s and S5KS is only 5 s after the S4KS.

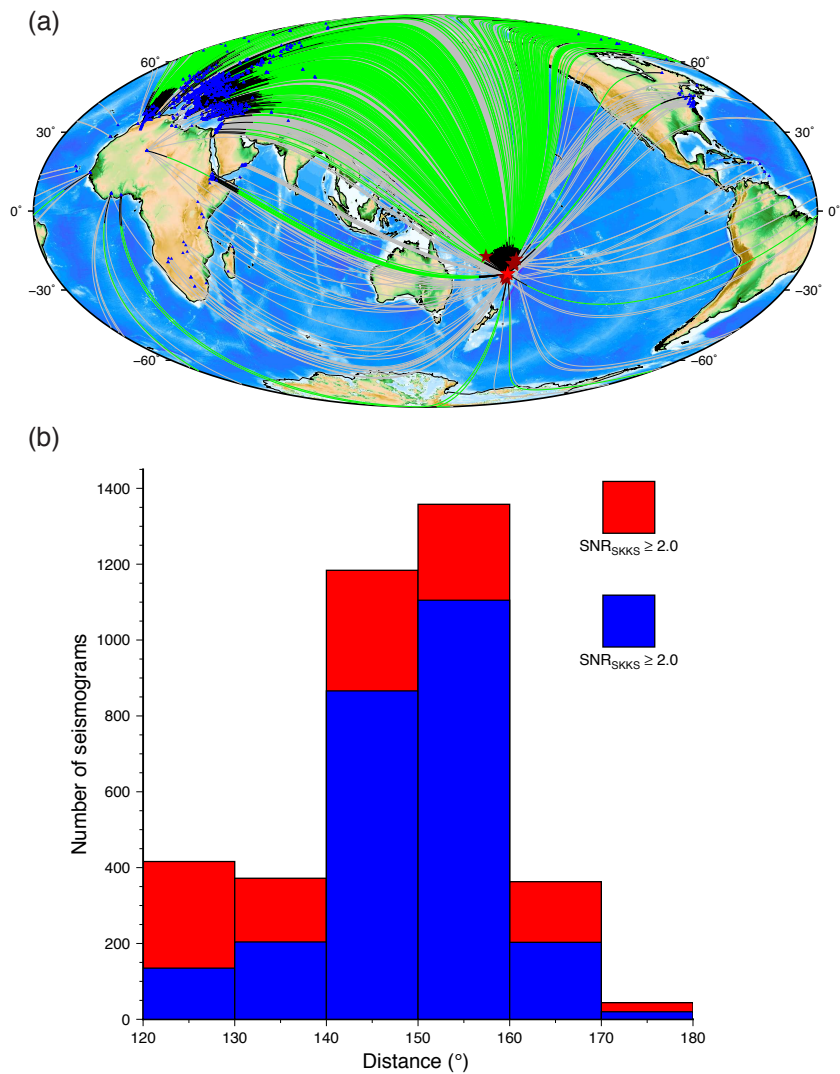


Figure 2: Map and histogram of clear SmKS data. (a) Map of good SKKS data ($\text{SNR} \geq 2.0$) from the ten earthquakes. The blue triangles and red stars show the stations and earthquakes, respectively. The lines connecting stations and earthquakes are ray paths of SKKS. The green lines show the ray paths of SKKS traveling in the outer core from the event #110729. (b) Histogram of SKKS data in (a). The blue bar portions correspond to SKKS data with high $\text{SNR} \geq 2.0$ and the red bar portions show the ones with $\text{SNR} < 2.0$.

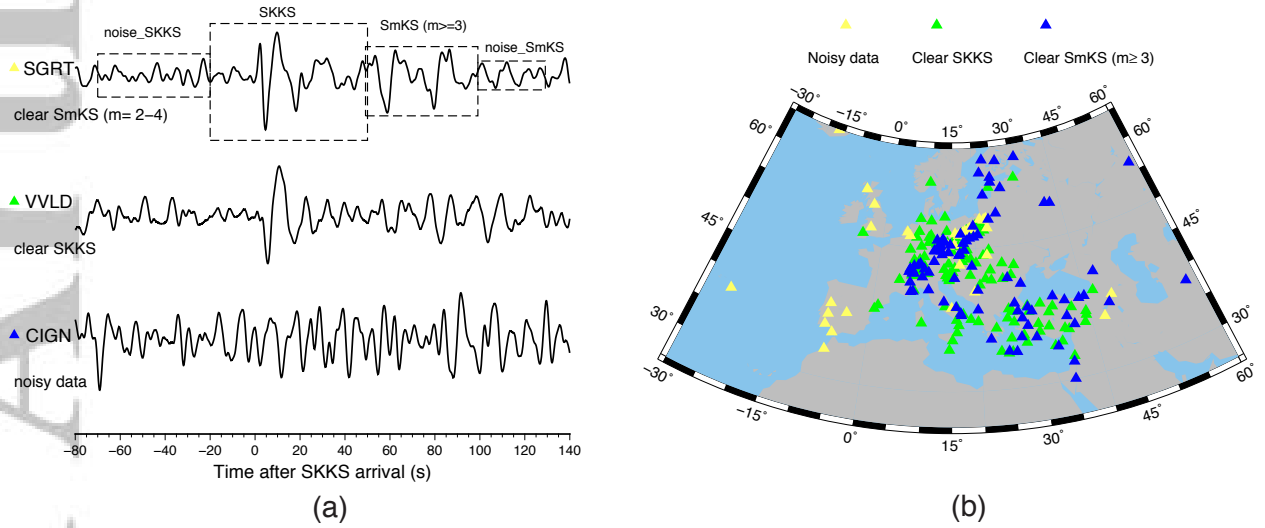


Figure 3: SmKS data from stations in Europe from event #071016. (a) An example of waveforms with poor SKKS with $\text{SNR} < 2.0$ (bottom panel), good SKKS with $\text{SNR} \geq 2.0$ only (middle panel), and high SNRs for both SmKS ($m=3$ and higher) and SKKS (top panel). The SNR of SKKS is defined as the peak-to-peak amplitude ratio of SKKS (20 s before to 50 s after the SKKS arrival predicted by PREM) to that of the noise (70 s to 20 s before the SKKS arrival). Similarly, the SNR of SmKS ($m \geq 3$) is obtained by measuring SmKS signals (0 s to 50 s after S3KS arrival) and the associated noise (50 s to 85 s after S3KS arrival). The time zero is the SKKS arrival predicted by PREM. (b) Map of stations in Europe from event #071016. Stations with noisy SKKS, good SKKS only and high SNRs for both SmKS ($m=3$ and higher) and SKKS are shown as yellow, green and blue triangles respectively.

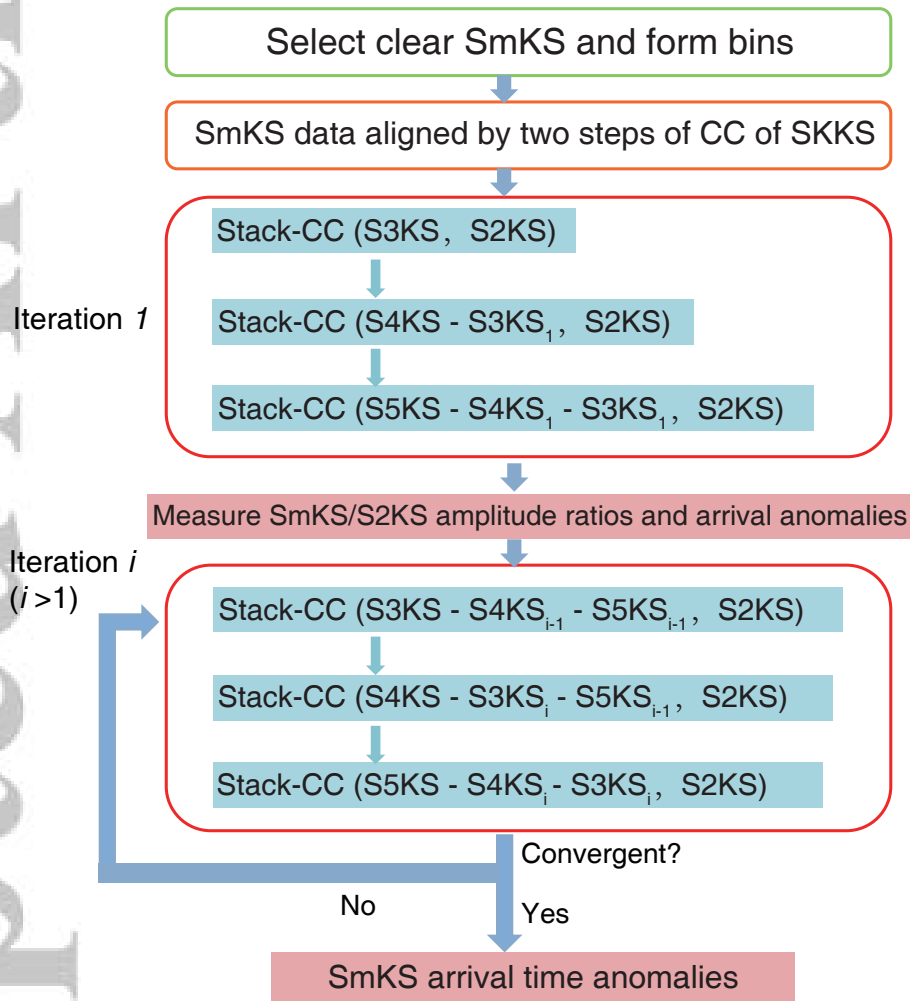


Figure 4: Workflow of the array-based iterative method.

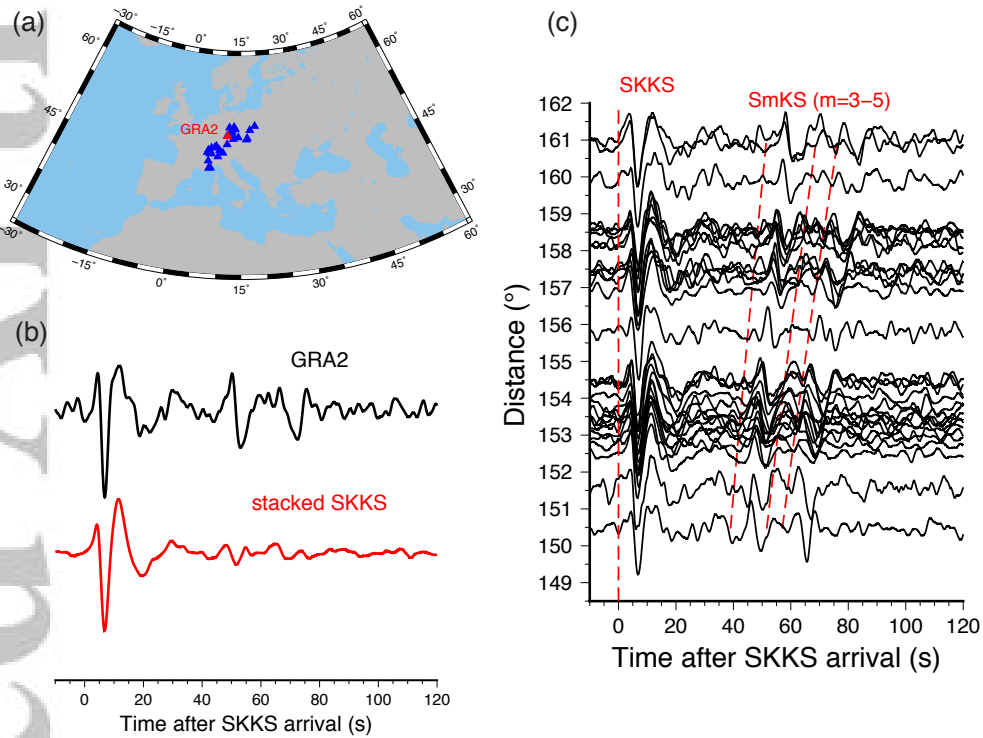


Figure 5: An example of aligning SKKS by two steps of cross-correlation. (a) A map of a bin of stations with clear SmKS from the event #071016. The other stations with clear SmKS are shown in Fig. 2b. (b) The SKKS waveforms from the reference station GRA2 (upper trace, epicentral distance of 154.4°) and stacked SKKS after alignment by CC with GRA2 (lower panel). (c) Distance profile of SmKS data (0.05-0.7 Hz) aligned on SKKS by two steps of CC. The corresponding stations are shown in (a). The time zero is the SKKS arrival. The other red dashed lines are the SmKS ($m=3-5$) arrivals predicted by PREM.

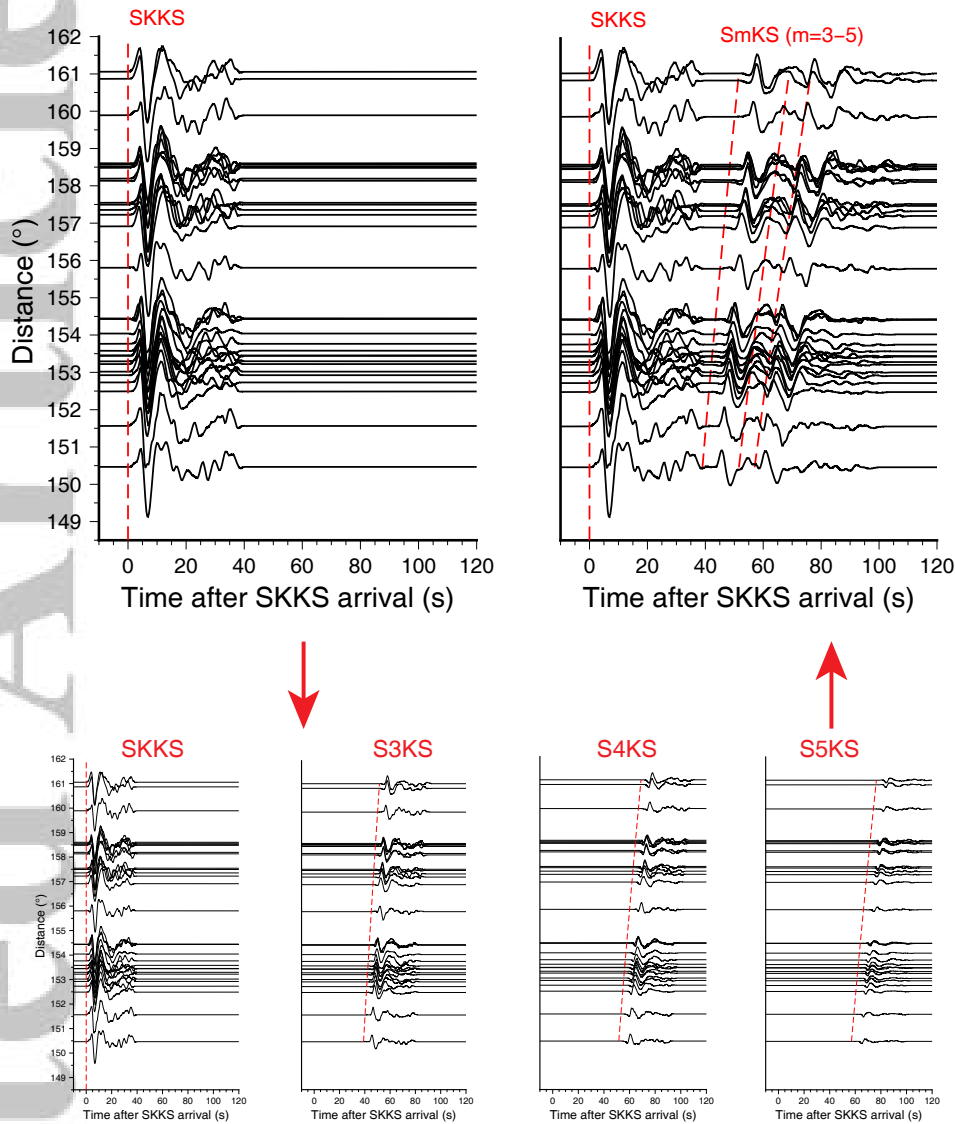


Figure 6: Making SmKS ($m=2-5$) synthetics using the SKKS data from the event #071016.

The upper left figure shows the cut-out and tapered SKKS waveforms (complete data shown in

Fig. 5c). Each sub-figure in the lower panel corresponds to the synthetics of individual SmKS

phase. We take the tapered SKKS data (upper left figure), scale them using given amplitude

ratios and apply the corresponding phase shift and time shift to form each SmKS phase. The

S3KS/SKKS amplitude ratio is given as 0.42 and its time delay is 1.13 s. For S4KS, the ampli-

tude ratio is 0.31 and the time delay is 2.25 s. For S5KS, the amplitude ratio is 0.14 and the

time delay is 2.39 s. These SmKS phases are added together to form the complete synthetics of

SmKS series (upper right figure). The dashed red line at the time zero in each figure is the SKKS

arrival, the same as Fig. 5c. The other red dashed lines are the SmKS ($m=3-5$) arrivals predicted

by PREM.

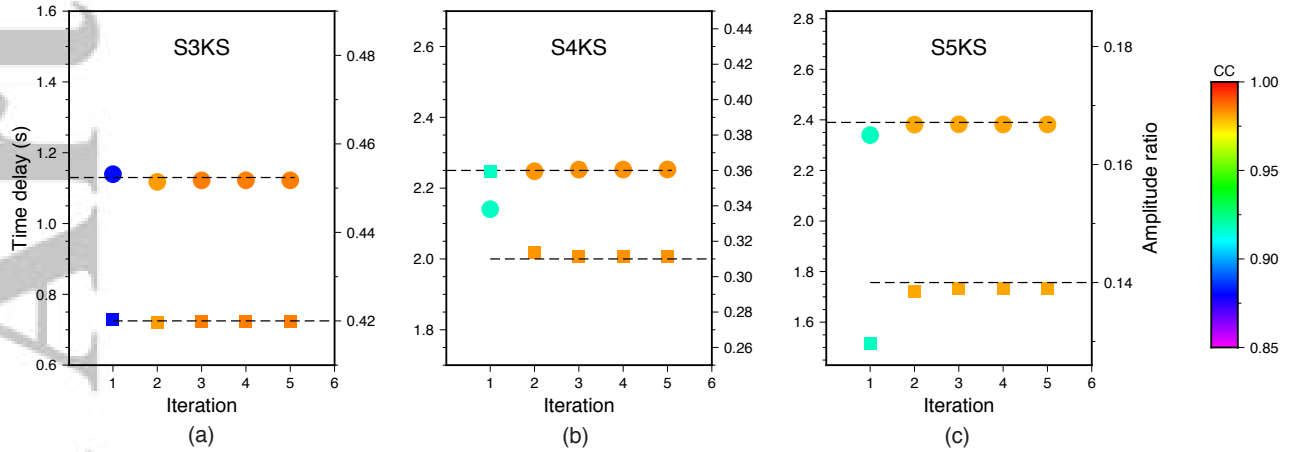


Figure 7: A synthetic test to validate the array-based iterative method. The colored circles indicate the measured time delay in each iteration. The colored squares are the measured amplitude ratios. The upper black dashed line in each figure is the prescribed time delay and the lower black dashed line corresponds to the given amplitude ratio. Note that the time delays are relative to SmKS-SKKS differential arrival times predicted by PREM. The color represents the CC values between the single SmKS phase and transformed SKKS (e.g. results of S5KS from the first four iterations shown in Fig. S2). Both time delays and amplitude ratios of S3KS, S4KS and S5KS converge to the input values after five iterations and this is also reflected in the high CC coefficients.

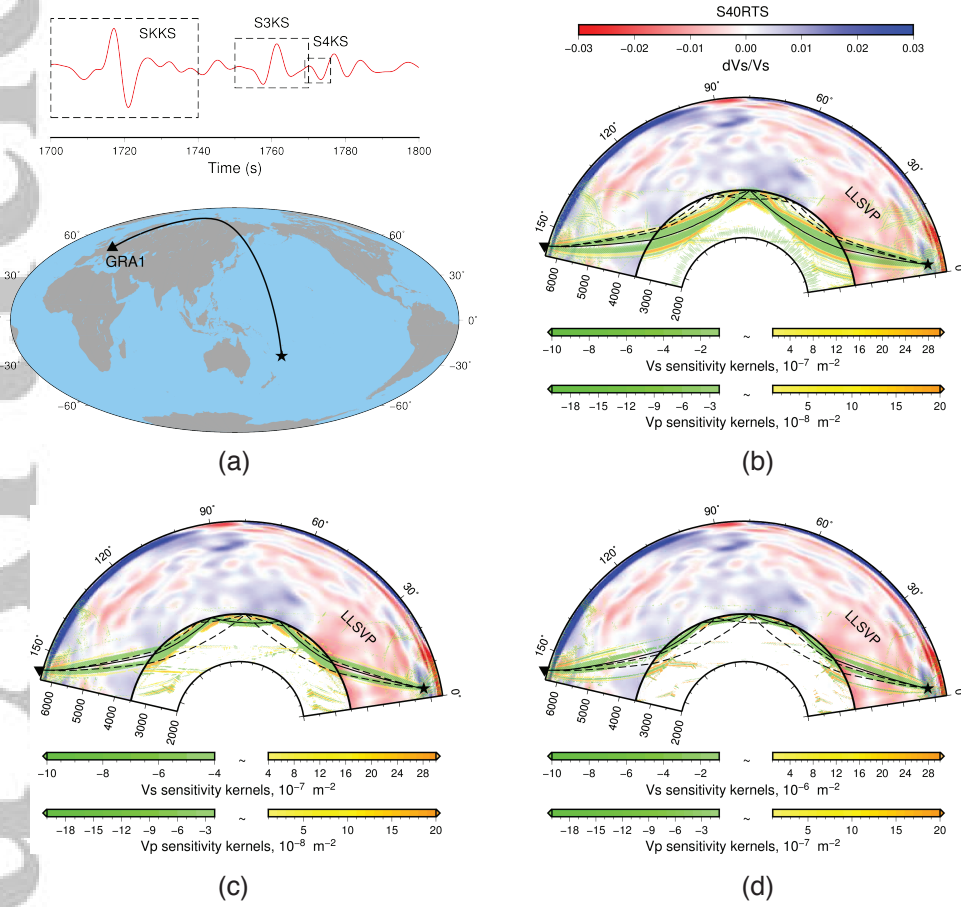


Figure 8: Map and travel time sensitivity kernels of SmKS ($m=2-4$) at station GRA1 from event #110729. (a) SEM synthetic seismogram (upper panel) and map (lower panel). The red line in the upper figure is the radial component synthetic seismogram of station GRA1 at 0.05–0.2 Hz. The triangle in the map shows the location of station GRA1 and the star is the centroid location of the event #110729. The black line in the map shows the great circle path of SmKS. The arrival times predicted by PREM are 1717.0 s for SKKS, 1758.5 s for S3KS and 1772.1 s for S4KS. The centroid time is 2.5 s, half of our re-estimated duration (Table S1), after the origin time for this event. (b) Travel time sensitivity kernels of SKKS. Sensitivity to Vs is shown in the mantle and to Vp in the core. The red-blue colors illustrate the depth cross-section of dVs/Vs (Vs perturbation) of the 3D model S40RTS. The green-yellow colors show the travel time sensitivity kernels of SKKS and its ray path is plotted with the black line. The dashed black lines are the ray paths of S3KS and S4KS. (c) Travel time sensitivity kernels of S3KS. (d) Travel time sensitivity kernels of S4KS.

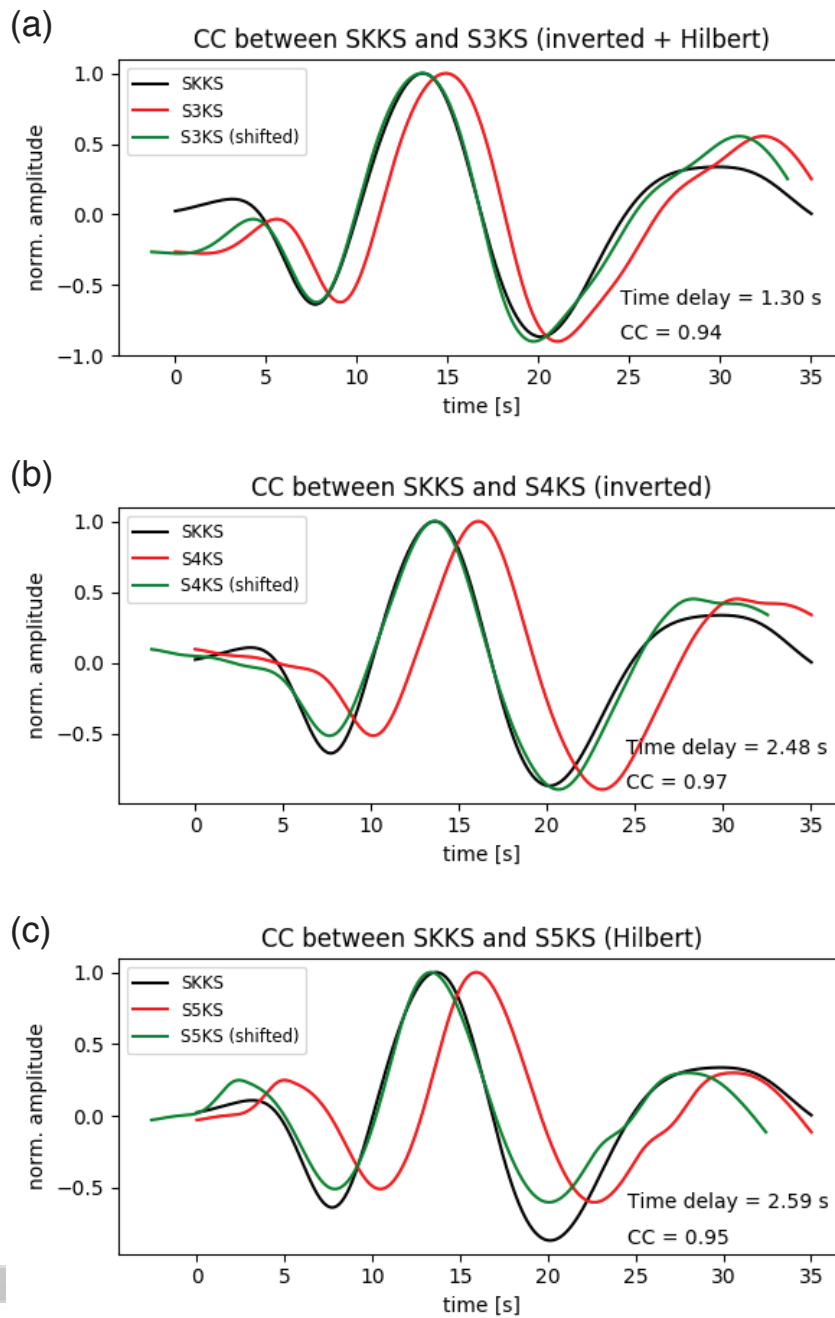


Figure 9: Time delays of S3KS, S4KS and S5KS measured on bin 4 data after five iterations from event #141101 (0.05-0.2 Hz). (a) CC between SKKS and S3KS (after Hilbert transform and polarity inverted). The black line is the stacked SKKS and the red line represents the stacked S3KS. The green line shows the shifted S3KS with the maximum CC value. The time shift between the red line and green line is 1.30 s and the corresponding CC value is 0.94. Note that the time delay is relative to S3KS-SKKS differential arrival time predicted by PREM. (b) CC between SKKS and S4KS (polarity inverted). (c) CC between SKKS and S5KS (after Hilbert transform).

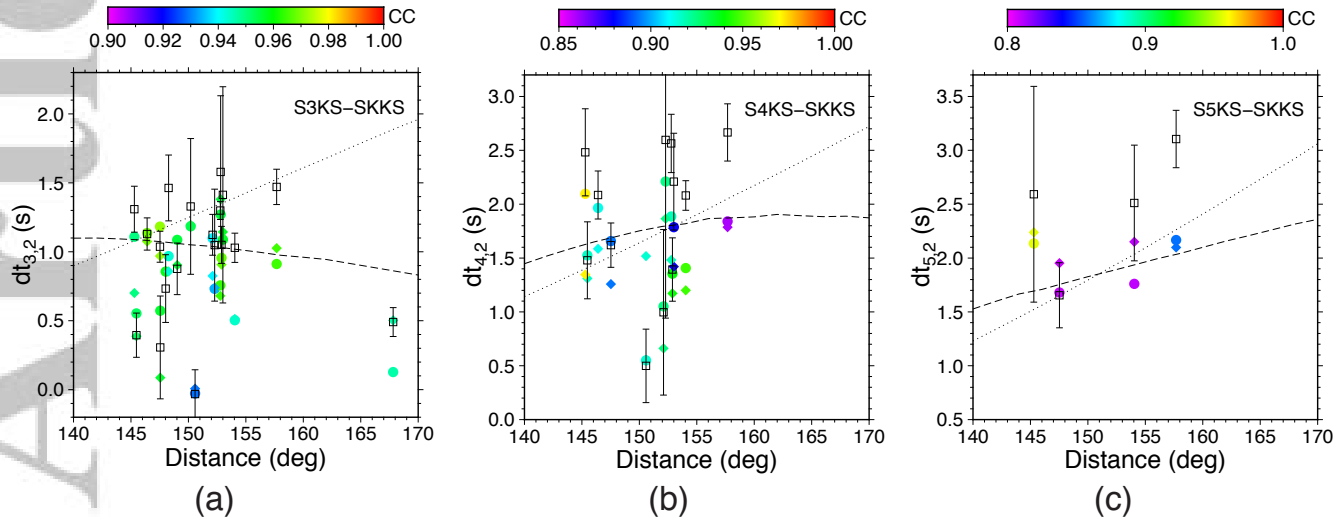


Figure 10: SmKS time delays measured at 0.05-0.2 Hz. The empty squares represent the SmKS ($m=3$ in a, 4 in b and 5 in c) time delays measured on the data. Note that error bars are symmetric and in a few cases extend beyond the limits of the figure. The solid circles are SmKS time delays after the 3D mantle structure corrections based on ray theory and using S40RTS model. The time delays are relative to SmKS-SKKS differential arrival times predicted by PREM. The solid diamonds are SmKS time delays after the corrections measured on the SEM synthetic seismograms made using S40RTS. The color shows the corresponding CC values measured on the data. More detailed information is displayed in Tables S3-5. The black dashed line in each figure is the corresponding SmKS time delay predicted by KHOMC (Kaneshima & Helffrich, 2013). The black dotted lines show the EPOC predictions. The source depth used in the KHOMC and EPOC predictions is 150 km. (a) S3KS time delays. (b) S4KS time delays. (c) S5KS time delays.